



Full Length Article

Zirconium hydride phase mapping in Zircaloy-2 cladding after delayed hydride cracking

Aaron W. Colldeweih^{a,*}, Malgorzata G. Makowska^{a,b}, Omaia Tabai^a, Dario Ferreira Sanchez^b, Johannes Bertsch^a

^a Laboratory for Nuclear Materials (LNM), Paul Scherrer Institut, Villigen PSI, Switzerland

^b Laboratory for Synchrotron Radiation and Femtochemistry (LSF), Paul Scherrer Institut, Villigen PSI, Switzerland

ARTICLE INFO

Keywords:

Delayed hydride cracking
X-ray diffraction (XRD)
Zirconium hydride
Zirconium alloys
Phase stability

ABSTRACT

Hydrogen uptake in zirconium alloys is a major limiting factor of nuclear fuel cladding as subsequent hydride precipitation can lead to potential cladding failure via delayed hydride cracking (DHC). The specific mechanisms of DHC have been a focus in earlier research, however there is still no clear definition of the resulting crystallography and limiting hydride sizes at various temperatures of crack propagation. In this work, a novel thermo-mechanical testing procedure was used to induce radially propagating DHC cracks in thin-walled cladding in a temperature range from 100 to 320 °C. Focused ion beam (FIB)- prepared lamellae were extracted from samples containing the arrested DHC crack for synchrotron micro-beam X-ray diffraction (μ XRD) mapping of crystallographic phases. The μ XRD phase maps provided information about the required hydride cluster size that would lead to fracture (less than 5 μ m), i.e. the critical hydride size. Phase mapping shows that DHC-responsible hydrides primarily consist of the δ phase, with slightly increased γ/δ ratios at lower cracking temperatures. In multilayer cladding, the liner material shows significantly increased ratios of γ -hydride, while on average, the δ -phase remains predominant. This work also highlights that the γ -hydride is indeed a stable zirconium hydride phase, which can precipitate during DHC propagation and within the inner liner of multilayer cladding.

1. Introduction

Zirconium alloys are used for nuclear fuel cladding in light and heavy water reactors due to their high corrosion resistance while maintaining sufficient mechanical properties and an economical neutron absorption cross-section [1]. Despite its corrosion resistance, there is an inevitable amount of cladding corrosion that occurs during its in-reactor lifetime due to the harsh water-coolant environment. As a result of corrosion, hydrogen is produced and partially picked up into the cladding. While there are additional sources of hydrogen, such as hydrogen water chemistry, that from corrosion is only observed to be picked up by the cladding [2]. Once the hydrogen has entered the cladding, it can be transported throughout the matrix given a number of driving forces, including diffusion based on Fick's law, the Sorret effect, and stress [3–5]. Once the hydrogen concentration exceeds the solubility limit, it will precipitate in the form of brittle hydrides. Many of the effects of hydrogen and hydrides in the presence of zirconium are within the scope of ongoing studies, some of which include the embrittlement of the

cladding and delayed hydride cracking (DHC) [6,7]. DHC is a crack growth phenomenon, in which hydrogen in solid solution migrates towards a location of higher tensile stress overcoming concentration gradients. Exceeding the solvus limit leads to precipitation of brittle hydrides. Subsequently, the hydride cluster can grow to a critical length [8,9], whereupon stresses in the material may lead to fracture and further crack propagation in repeated steps [10].

In boiling water reactors (BWR) there is increased interaction between the fuel pellet and cladding material compared to pressurized water reactors (PWR). The interaction is known as pellet-cladding interaction (PCI) and can lead to internal stress-corrosion cracking. In the 1980's a two-part multilayer cladding was created to mitigate PCI through the addition of an inner more ductile zirconium alloy layer. Such inner layer has been defined in the nuclear industry as an inner 'liner' and is joined through metallurgical methods to the primary structure of the fuel cladding, which is defined as the 'substrate' [11]. In the context of hydrogen uptake, the effects of a liner on hydrogen diffusion and precipitation kinetics has also been explored [12,13]

* Corresponding author.

E-mail address: aaron.colldeweih@psi.ch (A.W. Colldeweih).

<https://doi.org/10.1016/j.mtl.2023.101689>

Received 30 September 2022; Accepted 11 January 2023

Available online 12 January 2023

2589-1529/© 2023 The Authors. Published by Elsevier B.V. on behalf of Acta Materialia Inc. This is an open access article under the CC BY license (<http://creativecommons.org/licenses/by/4.0/>).

showing that the hydrogen is strongly attracted to the liner-substrate interface. The hydrogen subsequently precipitates at high concentrations within the liner material.

Cladding embrittlement through hydride precipitation is one of the most relevant concerns of fuel integrity during accident scenarios such as reactivity induced accidents (RIA) and loss of coolant accidents (LOCA), but also storage and transportation of spent nuclear fuel (SNF). During the dry storage and transport of SNF, thermo-mechanical conditions could potentially lead to DHC and put the fuel cladding mechanical integrity at risk. First, mechanical loads on the nuclear fuel cladding can originate from internal gas pressures within the fuel rod, pellet cladding mechanical interaction (PCMI), and those caused by handling and transportation operations [1]. Second, the fuel cladding undergoes various thermal cycles as the remaining decay heat from the fuel only slowly decreases and the fuel assembly transitions between various environments including cooling pools, packaging facilities, and storage in intermediate casks. The combination of the varying temperatures and stresses can promote the dissolution and diffusion of hydrogen to regions of high tensile stresses, leading to hydride precipitation at incipient cracks or other defects in the material.

As it is foreseen to store spent nuclear fuel up to several decades under dry storage conditions until a final repository will be available, the cladding temperature can largely vary depending on the amount of remaining decay heat. Thus, deeper understanding of the DHC phenomenon in a large range of temperatures is essential for safe storage [14]. This includes the fundamental understanding of hydrogen diffusion and hydride precipitation at various temperatures, whereas research on hydride precipitation and phase analysis has already been initiated [15–18]. However, due to the challenging test conditions and large amount of time required for low temperature tests, the DHC phenomena specifically at low temperatures have not been sufficiently studied up to now. Therefore, it is important to be able to distinguish the phases of zirconium hydrides as well as to quantify the hydride concentration with high-spatial resolution under various conditions. Among the various hydride phases that can occur in a stoichiometric range of ZrH_{1-2} , the fcc δ - $ZrH_{1.6-1.7}$ and fct γ - ZrH phases have been significantly reported upon [16–24]. One of the main open questions regarding the phases is whether the γ phase is stable or metastable. Literature states that at temperatures below a transition temperature of 180 °C, the hydrides could precipitate preferentially to the gamma phase [19,25], while above this temperature, hydrides should precipitate primarily to the delta phase, especially in the context of DHC [16]. Recent studies have shown a strong temperature [16] and cooling/quench rate [17] dependence of the γ/δ phase hydrides ratio within the region of a DHC crack flank. Barrow et al. has shown that δ -hydride is the core of the hydride encapsulated by a γ -phase. This work also states that the hydride precipitates and dissolves first in form an outer γ -hydride shell, which is followed by transition to a δ -phase. This pathway is associated with a lower accommodation energy of the γ -phase [18].

Recent literature has reported on various dependencies of DHC hydride precipitation showing the hydrogen concentration gradients around DHC cracks with neutron radiography measurements [15] as well as multi-physics modeling [26,27], giving hints to possible changes in phases or precipitation kinetics. As the temperature range which DHC can occur encompasses the precipitation temperatures for both δ and γ phases [28], a change in the mechanical properties between different hydride phases, like fracture toughness [22], could lead to a change in mechanical stability of the overall system depending on the temperature. Therefore, it is important to identify the hydride phases resulting from DHC over a range of temperatures encompassing all possible hydride phases.

The further understanding and identification of the hydride phases of DHC in a wide range of temperatures is crucial for development of numerical models for simulation of DHC phenomenon in fuel performance codes as the mechanical properties of the γ - and δ -hydrides phases can vary. Therefore, the primary objective of this study is to identify and

map the DHC-responsible hydride phases around an arrested crack tip within the substrate of Zr-alloy claddings with and without an inner liner. Moreover, hydride phases within and around the liner are analyzed.

This work presents the results of synchrotron μ XRD phase mapping of hydrides of four DHC cracks formed at various temperatures in cladding with and without an inner liner. In addition, the hydrides of a slow-cooled sample, acting as an unstrained reference, with an inner liner was measured. The results compliment recent neutron radiography of DHC cracks improving the spatial resolution of mapped hydrides and enabling phase identification [15].

2. Experimental

2.1. Materials

The material used in this study consisted of recrystallized (RXA) Zircaloy-2 cladding tubes from Westinghouse with (LK3/L) and without (LK3) an inner liner. The LK3/L tube sections have a nominal outer and inner diameter of 9.62×8.38 mm. The LK3 tube sections have an outer and inner diameter of 9.62×8.76 mm. Table 1 describes the composition of the two materials according to ASTM nuclear fuel cladding standards [29].

2.2. Sample preparation for DHC testing

The cladding material was hydrogenated in tube sections through gaseous charging using a Sievert's type apparatus and heat treated in order to homogenize the hydrogen distribution as described in the following references [12,15,30]. Specific hydrogen content was then measured through destructive testing, Hot Vacuum Extraction (HVE), using a LECO device at the Paul Scherrer Institut (PSI) resulting in average concentrations as seen in Table 2.

Notches were cut in the axial direction of the tube with a broaching tool using a standard steel razor blade. Notches were cut between 50 and 80 μ m deep with a root radius of approximately 30 μ m. The tube was cut into 4 mm long rings that were subsequently cut in half resulting in the final arc-shaped specimen shown in Fig. 1. The specimen dimensions resulted in a 4 mm thickness, B , and width, W , respective of the cladding wall thickness (0.43 mm). In the context of nuclear fuel cladding, the cladding wall thickness is equivalent to the specimen width, W , considering ASTM standard for bending tests [31]. The standard nomenclature for crack length is given as a .

2.3. DHC testing and slow-cooling procedures

The samples were first fatigue pre-cracked at room temperature according to previously reported procedures [15,32]. Subsequent to the propagation of the sharp initiation crack, the samples were mechanically unloaded and heated above the respective temperature of terminal solid solubility of hydrogen for dissolution (TSSD) and held for 1 h prior to cooling at 30 °C/h until reaching the test temperature [15,32–34]. Following the stabilization of the test temperature, the starting mechanical load l_0 was applied. Upon arrival to l_0 , the extensometer displacement was tared, and subsequent loading was iteratively redefined based on the current extensometer displacement (see Eq. (1)).

$$l_n = l_0 - r \times d \quad (1)$$

where l_n is the newly defined load, r is the linear load reduction rate, and d is the sample displacement. The initial values of l_0 were dependent on the cladding wall thickness, while r was defined on the basis of maintaining a stable crack growth. In other words, the sample was loaded with a constant loading scheme, where the load was iteratively redefined based on extensometer displacement on a given time interval. More specifically, the load was held constant during each interval, and

Table 1

ASTM specifications (weight%) of the Zircaloy-2 material used in this study. The LK3 alloy makes up the substrate of both materials (LK3 and LK3/L).

Alloy Name	Sn	Fe	Cr	Ni	O	Si	Zr
LK3	1.20–1.70	0.07–0.20	0.05–0.15	0.03–0.08	0.10–0.14	max. 0.009	bal.
Liner of (LK3/L)	max 0.3	max 0.07	–	–	–	–	bal.

Table 2

Hydrogen concentrations of the material used for DHC specimens.

Cladding Designation (-)	Test conditions	Measured Average (wppm H)	Standard Deviation (wppm H)
LK3/L	Slow-cooling (8 °C/h) 500→38 °C	143	22
LK3/L	DHC at 100 °C		
LK3	DHC at 100 °C		
LK3	DHC at 150 °C	201	15
LK3	DHC at 320 °C		

LK3 (without inner liner), LK3/L (with inner liner).

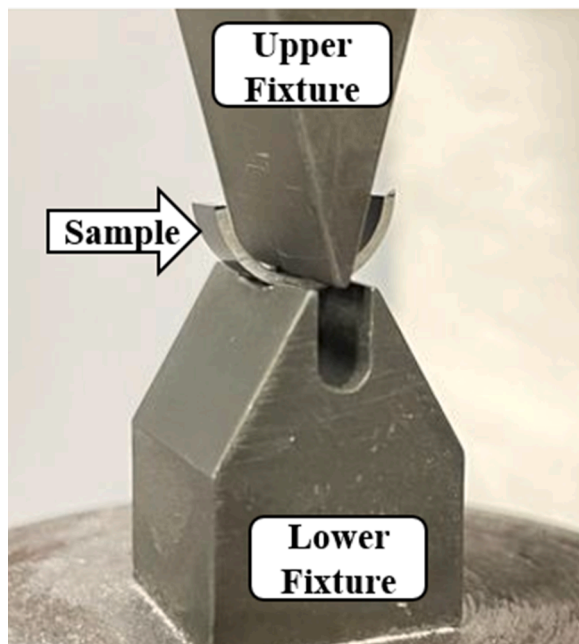


Fig. 1. Three-point bending fixture with an arc-shaped sample (0.6 mm cladding wall thickness) mounted for testing.

slightly reduced in the next interval relative to the extensometer displacement. With this loading scheme the sample was effectively unloaded in a continuous manner due to the high sensitivity in redefining the load. This loading scheme ensured a near constant stress intensity factor, K_I , during DHC, ranging from 10 to 20 MPa \sqrt{m} depending on the depth of the incipient fatigue crack. As the K_I value is near constant, and well below the fracture toughness of the hydrogen free material [35], subcritical cracking conditions are provided for DHC to occur. Further details on the loading scheme and test parameters can be found in the following reference in where the identical test set up is employed [32].

The slow-cooling test procedure utilized the same test facility as for the DHC testing, however without any mechanical load. Therefore, the heating and cooling was identically monitored and controlled so that the slow-cooled sample would act as an unstrained reference sample and be directly comparable to the DHC samples.

2.4. Sample preparation for μ -XRD

Subsequent to the DHC testing (step 1 in Fig. 2), samples were mounted to a cylindrical aluminum stub that fits inside a stainless steel tube with a pass-fit (like a piston and cylinder seen in Fig. 2 of step 2). With this device, a controllable amount of the sample was extended for accurate material removal. The next step (step 2), was to grind the inner diameter of the cladding. In step 3, the sample was remounted on its side, such that the crack cross section could be observed after grinding and polishing. The sample was polished on both sides to create a lamella thickness ($\sim 100 \mu\text{m}$) manageable for further FIB polishing where the extracted lamella contained a midsection of the original sample, thus representing a plane-strain crack cross section. The lamella was then mounted to a modified SEM stub with silver glue to the two mounting 'pillars' which enable an X-ray beam to pass (Steps 3 and 4). The samples were then further thinned in the same direction with a FIB in successive steps, with reduced current at each step (i.e. 45 nA, 27 nA, and 13 nA at 30 keV) to minimize FIB damage. The final thicknesses of the sample were between 10 – 35 μm .

2.5. μ -XRD experiment setup and data analysis

The Imaging of hydrides along crack flanks of a sample, required micron spatial resolution as the hydrides along DHC crack flanks can be very thin. Additionally, the sample dimensions were constrained to very thin cross sections ($<100 \mu\text{m}$), considering the material attenuation effects on the incident beam. However, due to the mechanical instability of a cracked region, the samples could not be produced thinner than several microns and therefore required dimensional optimization. Considering the aforementioned, the XRD-contrast microscopy technique available at microXAS beamline at PSI was the best-suited technique for phase identification throughout the DHC samples, allowing for phase distribution mapping with high spatial resolutions over a large region of interest (ROI).

The diffraction contrast imaging measurements were performed at the microXAS beamline of the Swiss Light Source [36]. The detector used in these experiments was the Dectris Eiger 4M [37,38]. The data was acquired during a raster scan of the sample with the X-ray beam focused down to 1 μm . In other words, the stage moved the sample in the plane normal to the beam over the selected (ROI) with a defined step size and acquisition time for each step. The scanning is also described in the following sections (see Fig. 3). Exact experimental conditions and scanning parameters can be found in Table 3.

2.5.1. Data processing

The first step in processing the raw data (images of Debye-Scherrer rings) involved using the python based library for fast azimuthal integration (PyFAI) using a generated calibration file in order to create the 1D diffraction patterns [39]. A LaB₆ standard was used for the creation of the aforementioned calibration file including information about the sample-detector setup geometry. An overview of the workflow is shown in Fig. 3.

Following the azimuthal integration, a stack of 1D XRD patterns was created. The stack of 1D XRD patterns was then loaded into a Matlab script where the XRD patterns were assigned to corresponding pixels in the ROI, thus generating separate images for each diffraction angle. It was then possible to evaluate a more refined ROI within the particular image that includes only, or mostly, specific crystalline phase, allowing to extract the information about the minor phases of interest. Such

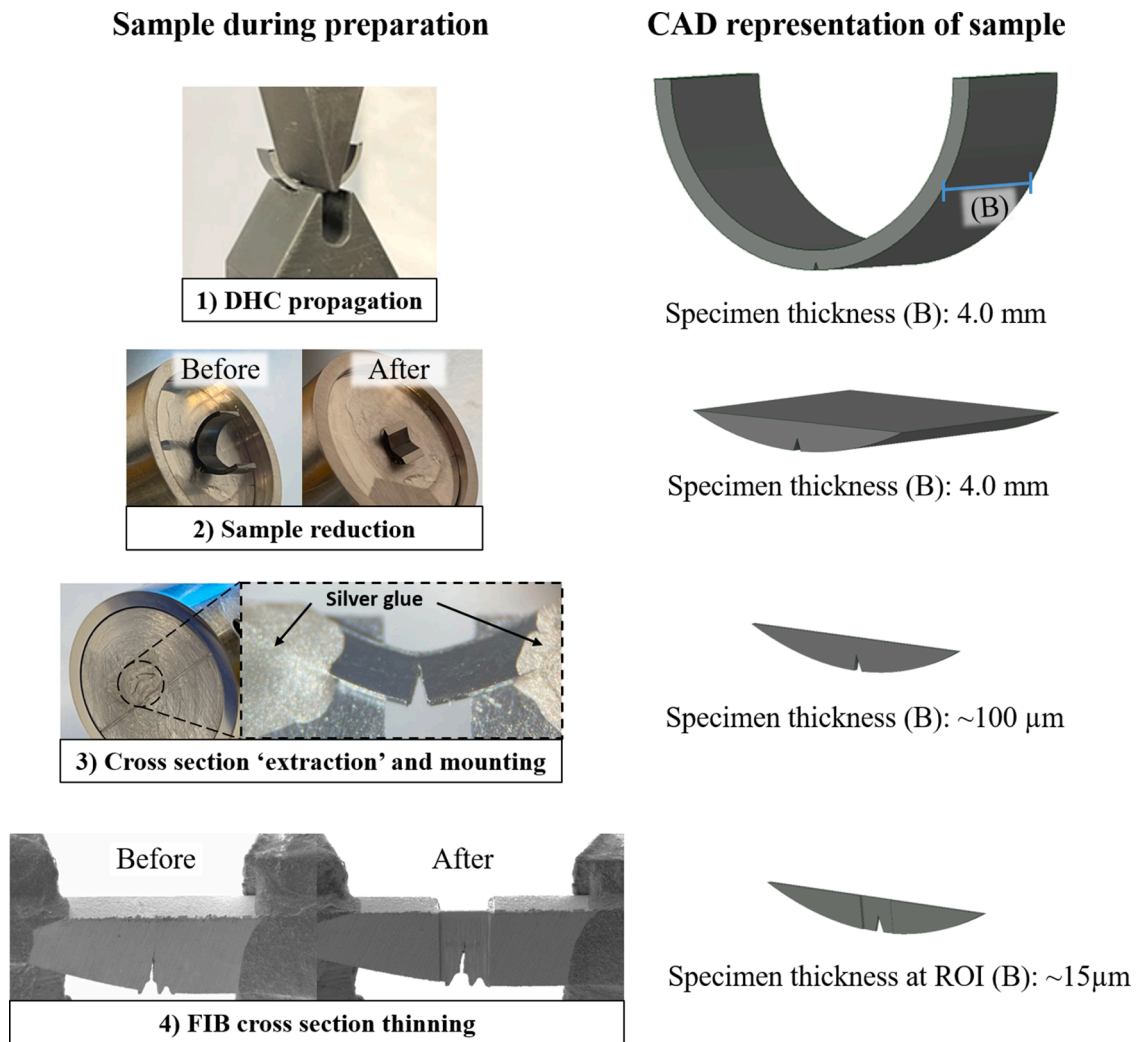


Fig. 2. The left column shows sample during the respective preparation step. In the right column the CAD drawing displays a representative sample. The sample preparation steps are as follows: (1) DHC propagation (2) excess material reduction (3) mechanical grinding and polishing to 'extract' a thin cross section of the crack within the plain strain region that is mounted on a holder using silver glue (4) SEM micrographs of the before and after of FIB milling to reduce the ROI to a thickness suitable for X-ray transmission.

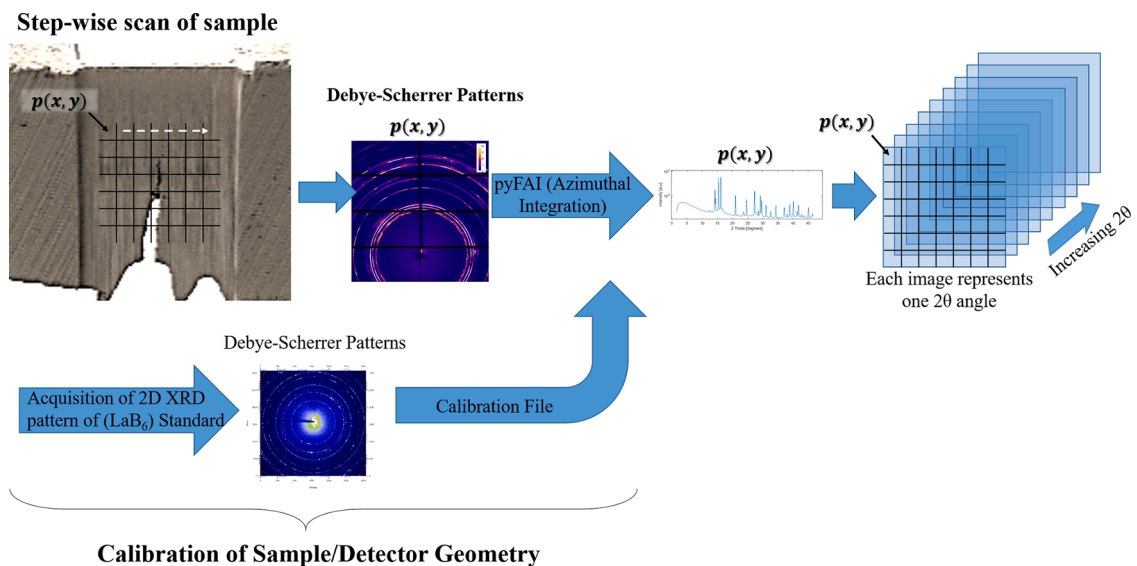


Fig. 3. Detailed workflow of imaging and data processing.

Table 3
Sample thickness and imaging parameters.

Test Conditions (Alloy)	Sample Thickness (μm)	Energy (keV)	Wavelength (Å)	Step Size (μm)	Dwell time (ms)	Beam Size (μm ²)	Area analyzed height x width (μm x μm)
Slow-cooling 500→38 °C (LK3/L)	35	17.95	0.6907	1.0	200	~1.0	646 × 100
DHC at 100 °C (LK3/L)	38						405 × 105
DHC at 100 °C (LK3)	16						250 × 60
DHC at 150 °C (LK3)	7	17.2	0.7209	0.5			390 × 100
DHC at 320 °C (LK3)	15						320 × 135

LK3 (without inner liner), LK3/L (with inner liner).

refined ROI is created by a user-defined polygon, as seen in Figs. 4 and 5 with red lines, in which specific hydride regions are captured.

The TOPAS software was utilized to fit models containing expected structures to the experimental diffraction patterns based on Rietveld refinement, which allowed for identification of the crystalline phases and their evaluation.

3. Results and discussion

3.1. Phase mapping

Based on the acquired diffraction patterns, phase maps, and light optical microscopy (LOM) (seen in Figs. 4 and 5), a number of observations were made including the spatial distribution of the hydrides around the crack tip and in the liner, identification of the hydride phase, and ratio of various phases. From the obtained images, the crack flank length containing a hydride phase was measured as the total DHC length, a_{DHC} . DHC velocities, V_{DHC} , were then calculated as the ratio (Eq. (2)) of a_{DHC} and the total DHC test time, t_{DHC} (see Table 4).

$$V_{\text{DHC}} = a_{\text{DHC}}/t_{\text{DHC}} \quad (2)$$

The crack velocity is constant over time in a mesoscale view and based on the process of continuous hydrogen diffusion and precipitation, but not in view of cracking of individual hydrides, which is known to be an iterative process. This is a standard way to define the DHC velocity. However, considering the difference in alloy, the crack velocities of these samples are very comparable with those values which can be found in literature giving confidence in the velocity measurement method and test procedure [33,34,40]. It is important to highlight the velocity comparison between the cladding material with and without an inner liner. While both sample crack velocities were extremely slow at 100 $^{\circ}\text{C}$, the material with an inner liner cracked at about one third of the velocity as the cladding without an inner liner. The decreased velocity is likely explained by the reduced hydrogen concentration in the substrate as a result of significant hydrogen diffusion towards, and precipitation within, the liner material during cooling to the test temperature [13]. It can otherwise be understood as a reduced hydrogen source for DHC as the crack propagates within the hydrogen-depleted substrate.

The crack velocities of the two low temperature (100 and 150 $^{\circ}\text{C}$) samples were extremely slow compared to the 320 $^{\circ}\text{C}$ sample. Therefore, it can be inferred that the time to reach a critically sized hydride cluster, which is the minimum region of material occupied by hydrides sufficient to initiate fracture, was much longer at low temperatures (100 and 150 $^{\circ}\text{C}$) as compared with 320 $^{\circ}\text{C}$. The slow rate of precipitation, and subsequent crack propagation, is primarily due to the small source of hydrogen in solid solution (equivalent terminal solid solubility of hydrogen for precipitation (TSSP): ~ 10 wppm H and ~ 20 wppm H for 100 $^{\circ}\text{C}$ and 150 $^{\circ}\text{C}$, respectively [41,42]) in combination with the slow rate of diffusion at low temperatures, as demonstrated in [43]. It should be noted that while DHC velocities are also expected to be slow above 300 $^{\circ}\text{C}$ [33,44], the limiting factors for high and low temperature DHC propagation must be considered when comparing the respective velocities. In this work, two temperature extremes for DHC are exhibited leading to velocities slower than those measured at ideal DHC conditions

found in literature [33]. At these temperature extremes, the limiting factor of slow hydrogen diffusion at low temperatures is greater than the plasticity of the zircaloy-2 at higher temperatures, leading to slower velocities at low temperatures. At higher temperatures (320 $^{\circ}\text{C}$), significantly higher amounts of hydrogen remain in solid solution (equivalent TSSP: 150–200 wppm H for 320 $^{\circ}\text{C}$ [41,42]), leading to a larger hydrogen source for DHC. Subsequently, the 320 $^{\circ}\text{C}$ sample displays much larger volumes of hydride precipitation along the DHC crack flanks. It can also be seen in the phase maps that there was sufficient hydrogen diffusion towards the crack, even in excess, as the hydride cluster extends away from the crack flanks near the onset point of DHC (tip of the fatigue zone) in the form of the stress field (see Fig. 4c).

In addition to the crack velocities, the exact location of the hydrides precipitation, under various conditions, can be identified with submicron resolution. In particular, it can be seen from LOM and XRD phase mapping (Figs. 4 and 5), at the lower test temperatures (100 and 150 $^{\circ}\text{C}$) that very thin hydride clusters have precipitated at the crack tip and crack flanks. This shows that thin hydride clusters are sufficient to induce DHC propagation, where at higher temperatures (320 $^{\circ}\text{C}$) larger hydride clusters may be necessary to induce DHC propagation, as it can be seen in the phase maps and LOM of Fig. 4. With these observation one can begin to infer the dimensions of a critically sized hydride cluster where the critically sized hydride cluster appears to be rather short (less than 5 μm) at low temperatures, as the extension of intact hydride is rather indistinguishable. With increased temperatures, the critical size appears to increase in width. However, the critical size may be disguised by excessive hydride precipitation when considering the hydrogen kinetics at elevated temperatures. Particularly, the increased amount of hydrogen in solid solution at higher temperatures will lead to increased hydride precipitation, which has previously been quantified using neutron radiography [15]. A secondary observation can be made about the hydride orientation around the crack tip of the samples. During the low temperature tests (100 and 150 $^{\circ}\text{C}$), the hydrogen within the material has had time to precipitate according to the solvus limits. As the cladding is strongly textured, it is expected that hydrides will precipitate in the circumferential direction (horizontally oriented in Fig. 4) as seen in the phase maps and LOM. However, at high temperatures (320 $^{\circ}\text{C}$) most of the hydrogen was still in solid solution prior to quenching, and after DHC propagation, therefore no significant circumferential hydrides have had a chance to precipitate.

In Fig. 5, the location of the hydrides within the two cladding samples with an inner liner (LK3/L) resulting from slow-cooling (8 $^{\circ}\text{C}/\text{h}$) and low temperature DHC (100 $^{\circ}\text{C}$) can be seen, in particular, with respect to the liner-substrate interface. The liner-substrate interface can be seen with high resolution where the two zones are delimited through the varied diffraction intensities in the phase map resulting from differing secondary phase particle (SPP) concentrations. The slow-cooled sample has been used as a reference sample in order to understand the precipitation of hydrides in the liner without external variables such as a stress field or an oncoming crack. These results specifically expand upon the neutron radiography studies on liner cladding under similar slow-cooling conditions where hydrogen concentrations were quantified in the liner and substrate showing the magnitude of hydrogen diffusion and precipitation within the liner [12,13]. The primary reason, as stated in the previous references, for the strong hydrogen

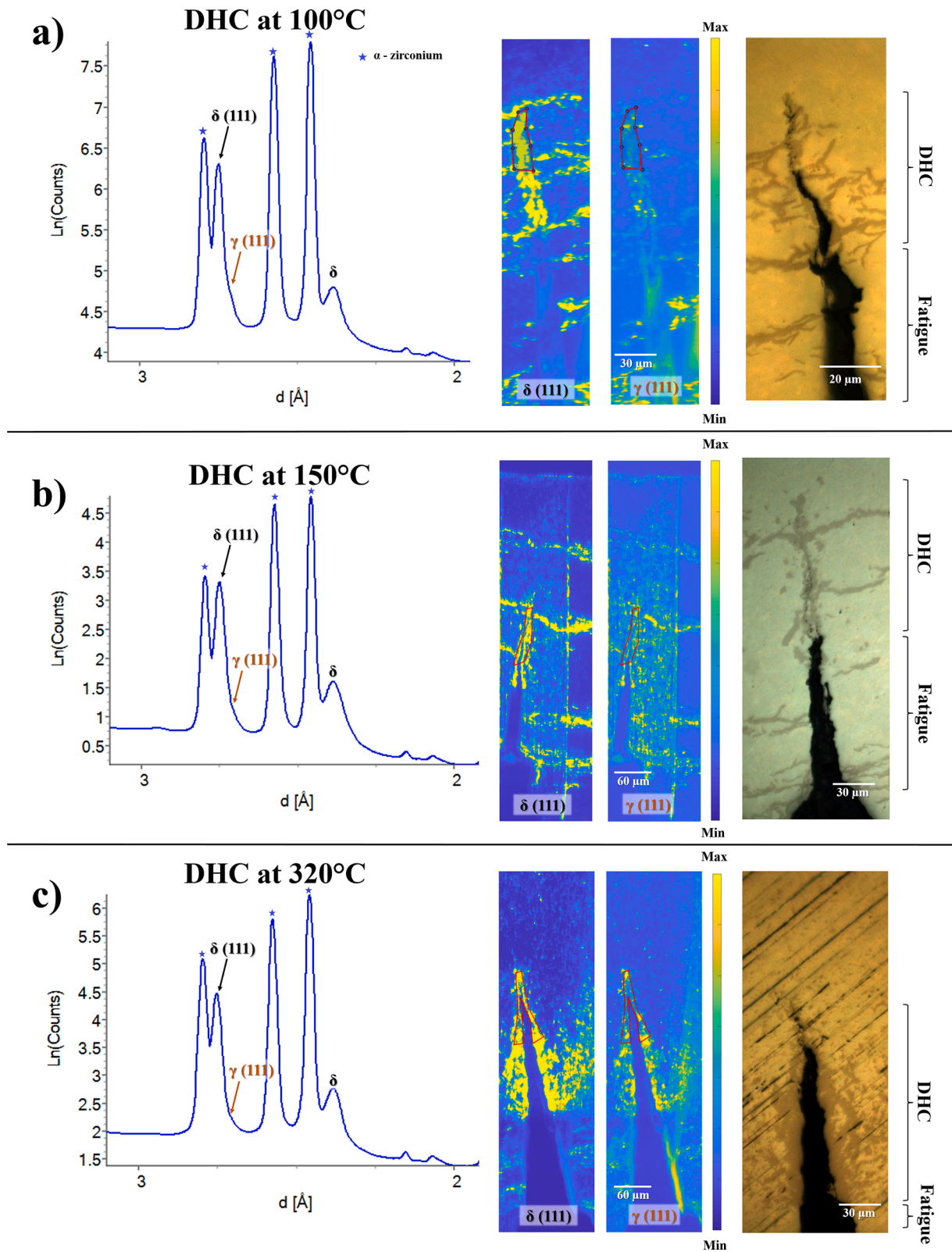


Fig. 4. The DHC cracks were propagated at (a) 100 °C, (b) 150 °C, and (c) 320 °C in fuel cladding without an inner liner (LK3) and contained an average hydrogen concentration of 201 wppm H. For each sample a)-c), the reduced diffraction patterns are shown to the left. The reduced diffraction pattern (left) represents the diffraction data only from the selected ROI, which is encompassed within the red polygon seen on the two phase maps (middle). The two phase maps represent the 2.76 and 2.71 Å d-spacing corresponding to the (111) lattice plane of the δ -hydride and γ -hydride respectively. The far right image is an LOM of the respective sample mapped with XRD.

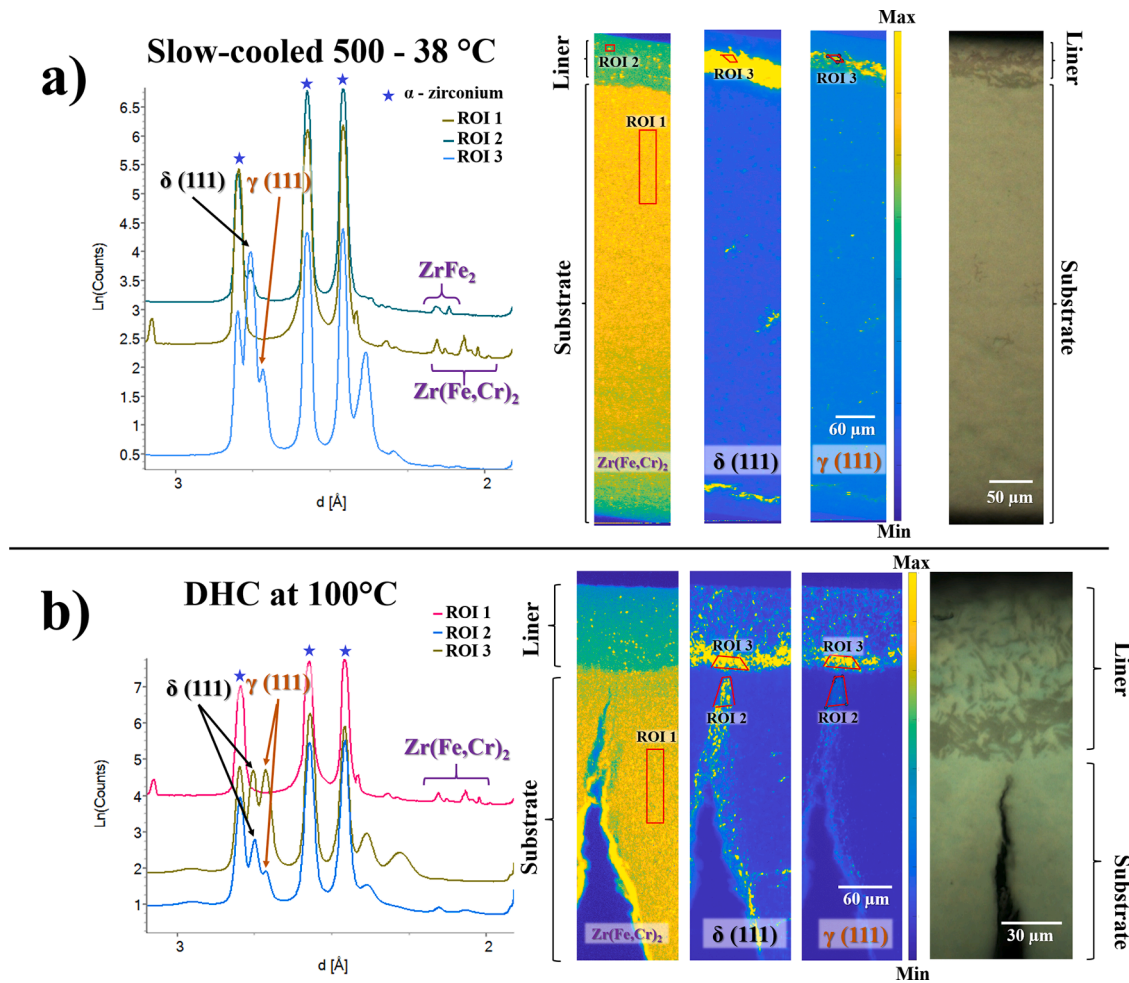


Fig. 5. Shown in (a) is a slow-cooled (8 °C/h) sample while in (b) the sample contains a DHC crack that was propagated at 100 °C. The material used was fuel cladding with an inner liner (LK3/L) and contained an average hydrogen concentration of 143 wppm H. For each sample, the reduced diffraction patterns are shown to the left representing the diffraction data from the selected ROI, which is encompassed within the red polygon seen on the three phase maps (middle). The three phase maps represent a Zr(Fe,Cr)_2 diffraction peak, as well as peaks at 2.76 and 2.71 Å d-spacing corresponding to the (111) lattice plane of the δ -hydride and γ -hydride respectively. The far right image is an LOM of the respective sample mapped with XRD.

Table 4

Summary of the DHC velocities from the tests in this work.

DHC Test Conditions (Alloy)	Velocity (m/s)
100 °C (LK3/L)	2.5E-11
100 °C (LK3)	7.7E-11
150 °C (LK3)	6.7E-10
320 °C (LK3)	6.9E-09

LK3 (without inner liner), LK3/L (with inner liner).

precipitation within the liner is due to chemical potential differences in the liner and substrate. As the hydrides begin to precipitate within the liner, the chemical potential is drastically reduced, resulting in hydrogen absorption out of the substrate. In the slow-cooled sample of Fig. 5a, ROI 1 and 2 were defined in order to highlight the SPP's within the substrate and liner respectively, while ROI 3 was selected to highlight the hydrides within the liner. It can be clearly seen that the some of the peaks related to the SPPs in ROI 2 are missing in ROI 1. As the composition of the liner and substrate is known (Table 1), it can be deduced that the remaining peaks of ROI 2, correspond to a phase of ZrFe_2 as chromium and nickel are not present in the liner material and tin does not create an SPP [45,46]. Inversely, the missing peaks might correspond to the ZrCr_2 SPP, however further investigation has not been done as SPP identification was not the primary focus of this work.

The phase maps in Fig. 5b displays the DHC crack region including the liner. Within the phase maps and LOM it is first apparent that a significant amount of hydrogen has precipitated within the liner. The second observation is that the hydride cluster along the crack flanks appears more dispersed compared to the samples seen in Fig. 4. However, it should be noted that the imaged ROI was about 38 μm thick (thicker than the other DHC sample ROIs). The increased thickness could result in a reduced average hydride signal as the rough crack flanks were likely not exactly parallel with the X-ray beam. Consequently, the hydride along the crack flanks may appear slightly blurred and broadened in the phase map. Considering the image blurring due to the sample thickness, as well as LOM, it can be assumed that the critical size of the hydride cluster must be just as small, or smaller than cladding without and inner liner as seen in Fig. 4a.

As a secondary observation within the liner cladding samples (Fig. 5), it might have been expected to see significant circumferential hydrides due to the slow-cooling and low test temperatures, as seen in the material without and inner liner (Fig. 4). However, there are little to no circumferential hydrides present in the substrate with the exception of the far side (away from the liner). While this is not the main focus of the study, it shows how significant the liner attraction is, to the degree that the substrate is nearly completely depleted of hydrogen before circumferential hydrides can precipitate.

In addition to the spatial distribution of the hydrides, the specific

hydride phase and can be determined through analysis of the selected diffraction patterns. However, in some cases, as in Fig. 4, the diffraction pattern alone was not sufficient to confirm the minor phases and required refined fitting.

3.2. Crystalline phase identification

Crystalline phase identification was performed by fitting a model to the diffraction pattern based on Rietveld refinement, which is necessary especially in case of a strong overlapping of peaks corresponding to different phases. The fitted models included structures of α -zirconium (ICSD 53,785), δ -hydride (ICSD 169,451), γ -hydride (ICSD 253,517). These enable high quality fitting and ability to calculate the ratio of the amount of the two hydride phases. It should be noted that due to large grain size and texture of the zirconium alloy (resulting in low zirconium alloy grain statistics), the absolute percentage of the α -zirconium structured phase, and subsequently hydride phases, could not be evaluated. The effects on the diffraction pattern of the zirconium alloy grain size and texture can be seen in the supplementary Fig. S1. However, the calculation of the ratio of the two hydride phases is reliable, as the grain size of the hydrides is significantly smaller providing a very good grain statistics in the measured data. For this reason, the whole diffraction patterns were fitted to identify the hydride crystalline structures and calculate the unit cell parameters. Next, the obtained parameters were used for fitting a diffraction pattern in a selected range for evaluation for the relative amounts of the hydride phases.

In Fig. 6 the results of curve fitting are shown for the three DHC cladding samples without an inner liner, where Fig. 7 presents the curving fitting of the two samples with an inner liner. The selected diffraction angles for curve fitting are highlighted in blue and represent the (1010) α -Zr, (111) δ -Hydride and (111) γ -Hydride peaks. It was

determined that while other δ -hydride peaks occurred in the diffraction pattern, the peak corresponding to the (111) plane was most visible and least obstructed by the overlapping α -zirconium structure diffraction reflections. Additionally, the reflection (111) of the γ -hydride appeared most visible as a shoulder in the (111) δ -hydride reflection.

According to the fitting the δ -hydride was the major phase around the DHC crack tip, while the γ -hydride phase was indeed detectable, particularly in low temperature (100 and 150 °C) DHC crack tips. This became more apparent when analyzing the ratios of γ/δ -hydrides (seen in Table 5) where there is a slight increase in the relative amount of γ -hydrides with decreasing temperature. The increased γ -hydrides phase at low temperatures correspond with findings in literature [20,25] where a δ - γ transformation take place below 180 °C. It should be noted that the uncertainty of the γ -hydride quantity at 320 °C was greater than the absolute amount giving doubt in the estimated amount. Considering the spatial resolution, while very high (sub-micron), might still be too low compared to what previous experiments have required (sub-nanometeric/high-resolution TEM) to identify very small regions of the γ -hydrides which encapsulated δ -hydrides [18]. However, the technique proves a viable method for the phase identification at the crack tip of submicron-sized features and phases.

Some XRD and EELS studies have reported dominating fractions of γ -hydrides which precipitated at lower temperatures or faster cooling rates [16–18,47]. In such XRD studies, relatively large X-ray beams (several hundred square microns) in reflection mode were utilized, thus making any phase mapping impossible. The EELS studies have shown in very small regions, at the atomic scale, γ - and δ -hydrides boarding one another. However, as the EELS technique allows for analysis of only small ROIs, phase mapping is limited in the total area (less than 10 μm^2). The analysis in this work does not support the findings of overwhelming amounts of γ -hydrides along low temperature DHC crack flanks.

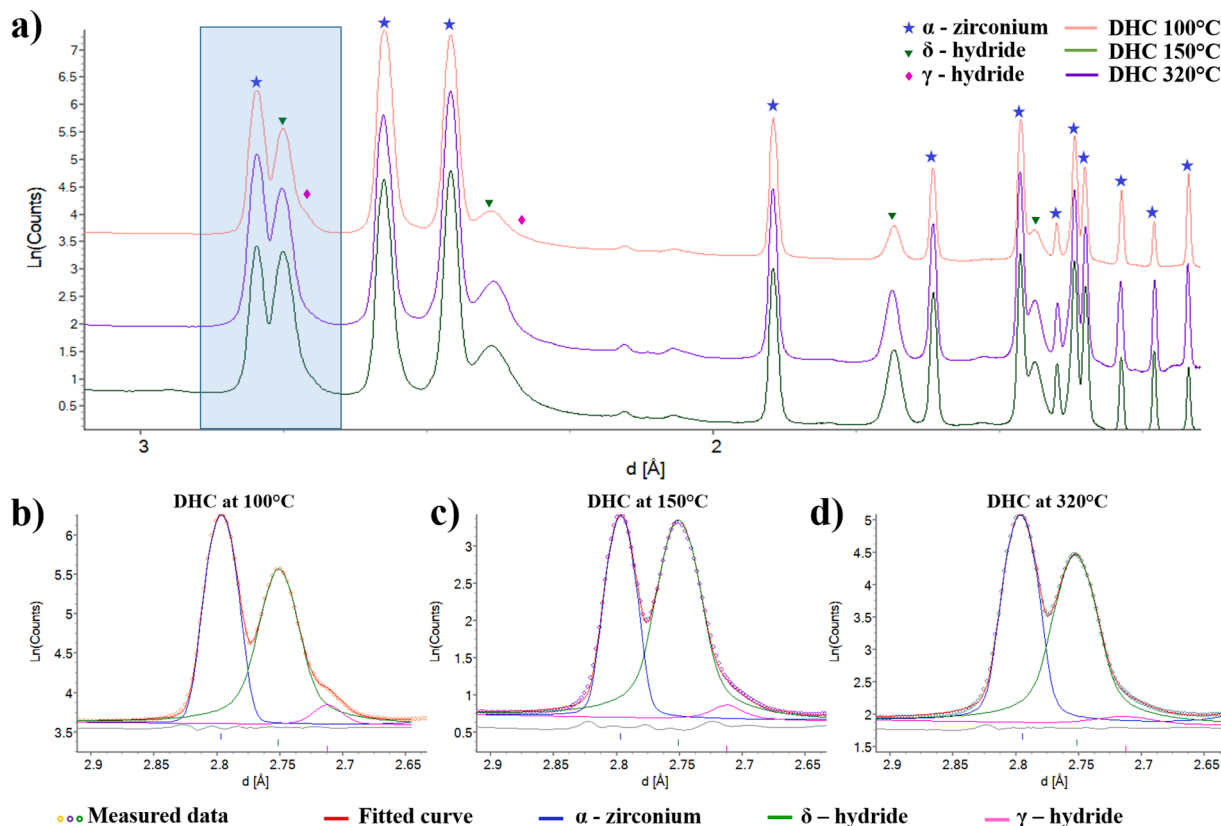


Fig. 6. (a) Diffractions patterns from the selected ROIs (DHC crack tip) outlined in the red frames seen in Fig. 4. The blue box in a) highlights the region used for curve fitting as shown in, (b) DHC at 100 °C, (c) DHC at 150 °C, and (d) DHC at 320 °C. The diffraction peaks used for curve fitting in (b), (c), and (d) represent the (1010) α -Zr, (111) γ - and δ -hydride planes. The individual theoretical phase patterns are shown with the experimental data and fitted curve.

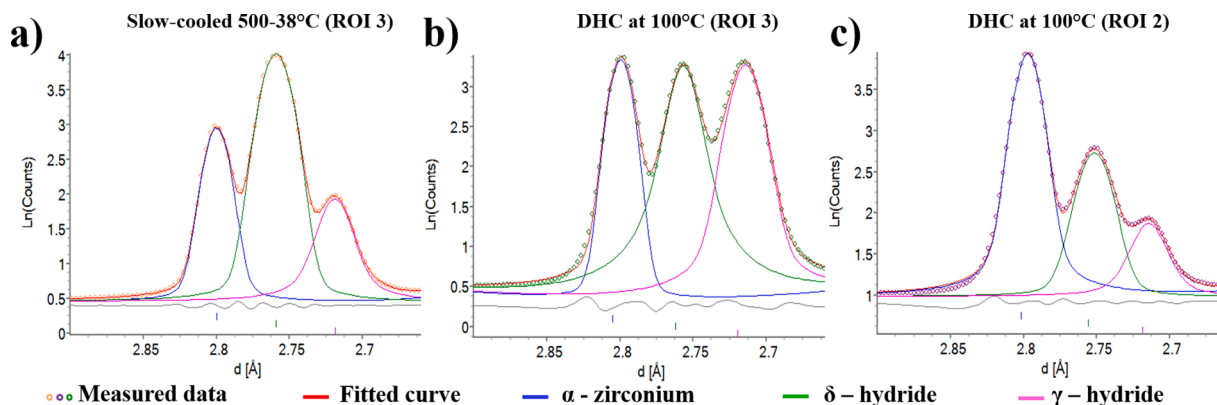


Fig. 7. Shown in (a) is the ROI 3 of the slow-cooled (8 °C/h) sample, (b) ROI 3 and (c) ROI 2 of DHC at 100 °C. The diffraction peaks used for curve fitting represent the (1010) α -Zr, (111) γ - and δ -hydride planes. The individual theoretical phase patterns are shown with the experimental data and fitted curve.

Table 5

Summary of relative concentrations of the contained phases in the selected ROI.

Test conditions (Alloy)	γ/δ -hydride ratio (%)
Slow-cooling 500–38 °C (LK3/L) – liner	14.4
100 °C (LK3/L) – liner (ROI 3)	121.5
100 °C (LK3/L) – crack tip (ROI 2)	46.3
100 °C (LK3)	3.7
150 °C (LK3)	2.0
320 °C (LK3)	1.5

LK3 (without inner liner), LK3/L (with inner liner).

However, the findings do show that γ -hydrides exist in a stable form, and possibly act as the precursory hydride precipitating at the DHC crack tip.

In Fig. 7, the curve fitting shows that the liner contains a very high amount of γ - and δ -hydride phase, while the α -zirconium structure is still present in such densely hydride concentrated regions. The quantitative analysis (see Table 5) shows that the liner contains distinct levels of the γ -hydride phase under slow-cooling conditions. Additionally, when undergoing stresses that lead to DHC, the liner material becomes more saturated in certain regions with γ -hydride than δ -hydrides. A number of studies have suggested that the more pure alloy, as shown within the inner liner of this study, will accommodate more γ -hydrides [19]. It has been suggested that the high-purity, i.e. lack of α -stabilizers, allow for the γ -hydride phase to be in equilibrium. Within this study, it appears that the strain within the liner, caused by deformation through DHC, can actually increase the amount of γ -hydride phase. This has also been investigated in literature, however under different conditions [48]. Additionally, the tip of the DHC crack in material with an inner liner contains more γ -hydride phase than DHC crack tips in material without an inner liner. As it well known that the hydrogen source for DHC within the substrate is low (due to the absorption into the liner) [13,33], the hydrides which do precipitate at the DHC crack can be postulated to be at minimum hydrogen-zirconium stoichiometry levels, resulting in higher amounts of the γ -hydride phase.

Table 5 presents the γ/δ -hydride ratios of the various ROIs defined in Figs. 4 and 5. It is apparent that the lower temperature DHC hydrides within the substrate have increased γ/δ -hydride ratios compared to elevated temperatures, while the liner material exhibits higher γ/δ -hydride ratios than the substrate under all conditions (reference and strained). Moreover, it was observed that not only the temperature, but also presence of stress affects the hydride phases formation within the liner. More specifically, the region of the liner material which had been strained (ahead of the crack tip) exhibits a significantly higher γ/δ -hydride ratio than the less strained regions of the liner away from the crack tip, as well as the unstrained liner region of the reference slow-cooled sample, indicating the effect of stress on the accommodation of γ -hydrides. While the quantities depend on the selected ROI, care was

taken to select representative regions with highest signals.

4. Conclusion

In this study, μ XRD phase mapping was used to analyze radial DHC cracks propagated in Zircaloy-2 fuel cladding with and without an inner liner at temperatures of 100, 150, and 320 °C. XRD contrast microscopy allowed to distinguish between the delta and gamma hydride phases within the Zr-alloy matrix and to map their distribution. The results show that the δ -hydride is the primary DHC-responsible hydride phase, while γ -hydrides are present, but at relatively low ratios. Phase maps showed that the majority of hydrides have precipitated within the liner material of the multilayer (LK3/L) cladding and form higher γ/δ -hydride ratios in strained regions of the liner compared to unstrained regions. The phase mapping also hints at the critical size of hydride cluster (less than 5 μ m) required to induce DHC while the increased hydride precipitation at elevated cracking temperatures (320 °C) may disguise the critical size of a hydride cluster due to potentially excess hydride precipitation.

The results have provided evidence that, while the γ -hydride is a minority phase in the DHC context, it is indeed found in a stable phase. Finally, a low concentration of γ -hydrides will likely have a low impact on DHC properties in the substrate of Zircaloy-2 fuel cladding, while further investigations on hydrides in the liner material should be performed.

Declaration of Competing Interest

The authors declare that they have no known competing financial interests or personal relationships that could have appeared to influence the work reported in this paper.

Acknowledgments

This work was funded by swissnuclear and Nagra (the Swiss National Cooperative for the Disposal of Radioactive Waste). The materials used in this work were provided by Westinghouse. Elisabeth Müller is thanked for her support with FIB preparations. Robert Zubler, Hans Kottman, Roger Schwenold, Andrej Bullemer, and Andreas Spahr are thanked for their technical support. The work is a part of the ongoing MIDAS program.

Supplementary materials

Supplementary material associated with this article can be found, in the online version, at doi:10.1016/j.mta.2023.101689.

References

- [1] INTERNATIONAL ATOMIC ENERGY AGENCY, "Waterside corrosion of zirconium alloys in nuclear power plants," IAEA-TECDOC-996, IAEA, Vienna (1998).
- [2] B. Cox, Effect of hydrogen injection on hydrogen uptake by BWR fuel cladding, *Electr. Power Res. Inst.* (1983), EPRI NP-3146.
- [3] P. Kreyns, W. Bourgeois, C. White, P. Charpentier, B. Kammenzind, D. Franklin, Embrittlement of reactor core materials, in: *Proceedings of the Zirconium in the Nuclear Industry: 14th International Symposium*, 1996, <https://doi.org/10.1520/stp16200s>, 758–758–25.
- [4] B.F. Kammenzind, D.G. Franklin, H.R. Peters, W.J. Duffin, Hydrogen pickup and redistribution in alpha-annealed Zircaloy-4, *ASTM Spec. Tech. Publ.* 1295 (1996) 338–370, <https://doi.org/10.1520/stp16180s>.
- [5] B.F. Kammenzind, B.M. Berquist, R. Bajaj, P.H. Kreyns, D.G. Franklin, The long-range migration of hydrogen through Zircaloy in response to tensile and compressive stress gradients, *ASTM Spec. Tech. Publ.* (1354) (2000) 196–233, <https://doi.org/10.1520/stp14301s>.
- [6] D. Hardie, The influence of the matrix on the hydrogen embrittlement of zirconium in bend tests, *J. Nucl. Mater.* 42 (3) (1972) 317–324, [https://doi.org/10.1016/0022-3115\(72\)90082-7](https://doi.org/10.1016/0022-3115(72)90082-7).
- [7] INTERNATIONAL ATOMIC ENERGY AGENCY, "Delayed hydride cracking of zirconium alloy fuel cladding," IAEA - TECDOC - 1649, IAEA, Vienna (2010).
- [8] D. Yan, R.L. Eadie, Approach to explain the stage I/II behaviour of the delayed hydride cracking velocity vs. KI curve for Zr-2.5 Nb, *Scr. Mater.* 43 (1) (2000) 89–94, [https://doi.org/10.1016/S1359-6462\(00\)00368-7](https://doi.org/10.1016/S1359-6462(00)00368-7).
- [9] J. Zhang, J. Zhu, S. Ding, L. Chen, W. Li, H. Pang, Theoretical models of threshold stress intensity factor and critical hydride length for delayed hydride cracking considering thermal stresses, *Nucl. Eng. Technol.* 50 (7) (2018) 1138–1147, <https://doi.org/10.1016/j.net.2018.07.001>.
- [10] M.P. Puls, *The Effect of Hydrogen and Hydrides on the Integrity of Zirconium Alloy Components*, Springer-Verlag, London, 2012 no. 1.
- [11] M. Dahlbäck, et al., The effect of liner component iron content on cladding corrosion, hydriding and PCI resistance, in: *Proceedings of the Zirconium in the Nuclear Industry: 14th International Symposium*, ASTM STP, 2004, pp. 873–895, <https://doi.org/10.1520/stp37539s>, yyyy.
- [12] W. Gong, et al., Hydrogen diffusion and precipitation in duplex zirconium nuclear fuel cladding quantified by high-resolution neutron imaging, *J. Nucl. Mater.* 526 (2019), 151757, <https://doi.org/10.1016/j.jnucmat.2019.151757>.
- [13] L.I. Duarte, F. Fagnoni, R. Zubler, W. Gong, P. Trtik, J. Bertsch, Effect of the inner liner on the hydrogen distribution of zircaloy-2 nuclear fuel claddings, *J. Nucl. Mater.* 557 (2021), 153284, <https://doi.org/10.1016/j.jnucmat.2021.153284>.
- [14] Switzerland, Swiss Federal Office of Energy, "Sectoral plan for deep geological repositories: conceptual part," Bern, (2008) <https://www.bfe.admin.ch/bfe/en/ho/me/versorgung/kernenergie/radioaktive-abfaelle/sachplan-geologische-tiefenlaager.exturl.html/aHROcHM6Ly9wdWJkY5iZmUuYWRTaW4uY2gvZW4vcHVibGljYX/Rpb24vZG93bmxyYWQvODE3MQ==.html> (accessed 12 April 2022).
- [15] A.W. Colldeweih, F. Fagnoni, P. Trtik, R. Zubler, M.A. Pouchon, J. Bertsch, Delayed hydride cracking in Zircaloy-2 with and without liner at various temperatures investigated by high-resolution neutron radiography, *J. Nucl. Mater.* 561 (2022), 153549, <https://doi.org/10.1016/j.jnucmat.2022.153549>.
- [16] C.E. Coleman, G.A. McRae, A. Buyers, S. Hanlon, Gamma-zirconium hydride on DHC fracture surfaces is a legitimate stable phase, not a metastable phase, *J. Nucl. Mater.* 548 (2021) 1–5, <https://doi.org/10.1016/j.jnucmat.2021.152839>.
- [17] E. Tulk, M. Kerr, M.R. Daymond, Study on the effects of matrix yield strength on hydride phase stability in Zircaloy-2 and Zr 2.5 wt% Nb, *J. Nucl. Mater.* 425 (1–3) (2012) 93–104, <https://doi.org/10.1016/j.jnucmat.2011.10.051>.
- [18] A.T.W. Barrow, A. Korinek, M.R. Daymond, Evaluating zirconium-zirconium hydride interfacial strains by nano-beam electron diffraction, *J. Nucl. Mater.* 432 (1–3) (2013) 366–370, <https://doi.org/10.1016/j.jnucmat.2012.08.003>.
- [19] L. Lanzani, M. Ruch, Comments on the stability of zirconium hydride phases in Zircaloy, *J. Nucl. Mater.* 324 (2–3) (2004) 165–176, <https://doi.org/10.1016/J.JNUCMAT.2003.09.013>, Jan.
- [20] J.H. Root, W.M. Small, D. Khatamian, O.T. Woo, Kinetics of the δ to γ zirconium hydride transformation in Zr-2.5Nb, *Acta Mater.* 51 (7) (2003) 2041–2053, [https://doi.org/10.1016/S1359-6454\(03\)00004-1](https://doi.org/10.1016/S1359-6454(03)00004-1).
- [21] M.A.V. Alvarez, J.R. Santisteban, G. Domizzi, J. Almer, Phase and texture analysis of a hydride blister in a Zr-2.5Nb tube by synchrotron X-ray diffraction, *Acta Mater.* 59 (5) (2011) 2210–2220, <https://doi.org/10.1016/j.actamat.2010.12.024>.
- [22] K.G. Barraclough, C.J. Beevers, Some observations on the deformation characteristics of bulk polycrystalline zirconium hydrides - part 1 the deformation and fracture of hydrides based on the δ -phase, *J. Mater. Sci.* 4 (6) (1969) 518–525, <https://doi.org/10.1007/BF00550212>.
- [23] D.O. Northwood, Gamma and delta hydrides in zirconium alloys, *J. Less Common Met.* 48 (1) (1976) 173–175, [https://doi.org/10.1016/0022-5088\(76\)90243-5](https://doi.org/10.1016/0022-5088(76)90243-5).
- [24] M.S. Blackmur, et al., Zirconium hydride precipitation kinetics in Zircaloy-4 observed with synchrotron X-ray diffraction, *J. Nucl. Mater.* 464 (2015) 160–169, <https://doi.org/10.1016/j.jnucmat.2015.04.025>.
- [25] J.H. Root, R.W.L. Fong, Neutron diffraction study of the precipitation and dissolution of hydrides in Zr-2.5Nb pressure tube material, *J. Nucl. Mater.* 232 (1) (1996) 75–85, [https://doi.org/10.1016/0022-3115\(96\)00379-0](https://doi.org/10.1016/0022-3115(96)00379-0).
- [26] Z. Xia, J. Zhang, Q. Tong, S. Ding, Multi-physics modeling of delayed hydride cracking in zirconium alloys, *J. Mech. Phys. Solids* 132 (2019), <https://doi.org/10.1016/j.jmps.2019.07.020>.
- [27] G. Ding, et al., Effects of irradiation on the multi-field coupling delayed hydride cracking behavior of zirconium alloys, *J. Nucl. Mater.* 563 (2022), 153605, <https://doi.org/10.1016/j.jnucmat.2022.153605>.
- [28] D.O. Northwood, U. Kosasih, Hydrides and delayed hydrogen cracking in zirconium and its alloys, *Int. Met. Rev.* 28 (1) (1983) 92–121, <https://doi.org/10.1179/imtr.1983.28.1.92>.
- [29] R.F. Cladding, Standard specification for wrought Zirconium alloy seamless tubes for nuclear, *Focus* 14 (2002) 1–20, <https://doi.org/10.1520/B0811-13R22E01>. Copyright (Madison)Reapproved 2017.
- [30] G. Domizzi, L. Lanzani, P. Coronel, P. Bruzzoni, Supercharging of zircaloy-4, *J. Nucl. Mater.* 246 (2–3) (1997) 247–251, [https://doi.org/10.1016/S0022-3115\(97\)00147-5](https://doi.org/10.1016/S0022-3115(97)00147-5).
- [31] ASTM Standard E1820, 2012 "Standard Test Method for Measurement of Fracture Toughness," ASTM International, West Conshohocken, PA, 2012, doi:10.1520/E1820-13, www.astm.org.
- [32] A.W. Colldeweih, J. Bertsch, Effect of temperature and hydrogen concentration on the threshold stress intensity factor of radial delayed hydride cracking in fuel cladding, *J. Nucl. Mater.* 565 (2022) 153737, <https://doi.org/10.1016/j.jnucmat.2022.153737>.
- [33] A.W. Colldeweih, et al., 'Radial delayed hydride cracking in irradiated Zircaloy-2 cladding: advanced characterization techniques, in: *Proceedings of the Zirconium in the Nuclear Industry: 20th International Symposium*, ASTM STP1645, 2022.
- [34] A.W. Colldeweih, (2022) "Delayed hydride cracking in irradiated and unirradiated Zircaloy-2 cladding," *École Polytechnique Fédérale de Lausanne*, Lausanne.
- [35] F.H. Huang, Fracture toughness evaluation for Zircaloy-2 pressure tubes with the electric-potential method, *ASTM Spec. Tech. Publ.* (1204) (1993) 182–198, <https://doi.org/10.1520/stp12729s>.
- [36] C.N. Borca, et al., The microXAS beamline at the swiss light source: towards nano-scale imaging, *J. Phys. Conf. Ser.* 186 (2009) 8–11, <https://doi.org/10.1088/1742-6596/186/1/012003>.
- [37] A. Forster, "EIGER detectors in biological crystallography," [White Paper] (19 May 2016) https://media.dectris.com/White_Paper_EIGER_May2016.pdf.
- [38] I. Johnson, et al., Eiger: a single-photon counting X-ray detector, *J. Instrum.* 9 (5) (2014), <https://doi.org/10.1088/1748-0221/9/05/C05032>.
- [39] J. Kieffer, D. Karkoulis, PyFAI, a versatile library for azimuthal regrouping, *J. Phys. Conf. Ser.* 425 (PART 20) (2013), <https://doi.org/10.1088/1742-6596/425/20/202012>.
- [40] S.M. Hanlon, G.A. McRae, C.E. Coleman, A. Buyers, Fracture of gamma and delta hydrides during delayed hydride cracking, in: *Proceedings of the Zirconium Nuclear Industry 19th International Symposium*, 2021, pp. 762–785, <https://doi.org/10.1520/stp162220190023>.
- [41] R.N. Singh, S. Mukherjee, A. Gupta, S. Banerjee, Terminal solid solubility of hydrogen in Zr-alloy pressure tube materials, *J. Alloy. Compd.* 389 (1–2) (2005) 102–112, <https://doi.org/10.1016/j.jallcom.2004.07.048>.
- [42] K. Une, et al., The terminal solid solubility of hydrogen in irradiated Zircaloy-2 and microscopic modeling of hydride behavior, *J. Nucl. Mater.* 389 (1) (2009) 127–136, <https://doi.org/10.1016/j.jnucmat.2009.01.017>.
- [43] A.T. Motta, et al., Hydrogen in zirconium alloys: a review, *J. Nucl. Mater.* 518 (2019) 440–460, <https://doi.org/10.1016/j.jnucmat.2019.02.042>.
- [44] T. Kubo, Y. Kobayashi, H. Uchikoshi, Measurements of delayed hydride cracking propagation rate in the radial direction of Zircaloy-2 cladding tubes, *J. Nucl. Mater.* 427 (1–3) (2012) 18–29, <https://doi.org/10.1016/j.jnucmat.2012.04.012>.
- [45] C. Proff, *Microstructural Aspects of the Oxidation of Zirconium*, Université de Grenoble, 2011.
- [46] M. Bojinov, et al., *In-situ* studies of the oxide film properties on BWR fuel cladding materials, *ASTM Spec. Tech. Publ.* (1467) (2005) 367–385, <https://doi.org/10.1520/stp37516s>.
- [47] O.T. Woo, G.J.C. Carpenter, Identification of zirconium hydrides by electron energy loss spectroscopy, *Scr. Metall.* 20 (3) (1986) 423–426, [https://doi.org/10.1016/0036-9748\(86\)90172-9](https://doi.org/10.1016/0036-9748(86)90172-9).
- [48] A. Steuwer, J.R. Santisteban, M. Preuss, M.J. Peel, T. Buslaps, M. Harada, Evidence of stress-induced hydrogen ordering in zirconium hydrides, *Acta Mater.* 57 (1) (2009) 145–152, <https://doi.org/10.1016/j.actamat.2008.08.061>.